Finite Elements in Analysis and Design 225 (2023) 104008

Contents lists available at ScienceDirect

Finite Elements in Analysis & Design

journal homepage: www.elsevier.com/locate/finel

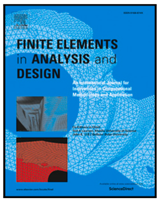

Three-dimensional modelling of in-isolation tensile response of geogrids using hyperbolic constitutive models

Lucas Paiva [a,*], Margarida Pinho-Lopes [a,c], Robertt Valente [b], António Miguel Paula [a,c,d]

[a] *RISCO, Department of Civil Engineering, University of Aveiro, Portugal*
[b] *TEMA, Department of Mechanical Engineering, University of Aveiro, Portugal*
[c] *CONSTRUCT-GEO, Department of Civil Engineering, Faculty of Engineering, University of Porto, Portugal*
[d] *Instituto Politecnico de Braganca, Portugal*

ARTICLE INFO

Keywords:
Geogrids
ABAQUS
Numerical modelling
Plasticity
Softening
Fracture

ABSTRACT

Numerical modelling of geogrids is a challenging task, with extruded geogrids often presenting complex geometries and nonlinear tensile response even at low strain rates. In this study, three-dimensional (3D) models were developed in ABAQUS to investigate the in-isolation tensile response of extruded geogrids, accounting for a detailed geometric discretization. Hyperbolic constitutive models were used to represent the nonlinear tensile response, including fracture simulation. A benchmarking exercise was initially performed using the literature data to assess the main numerical modelling parameters for a precise and time efficient simulation. Then, a case study composed of three extruded geogrids were used to validate the model. Particular emphasis was given on the data treatment of the case study, namely with the development of a data-driven model to obtain the most representative load strain curve from experimental specimens. The modelling approach proposed in this study was capable of capturing the in-isolation tensile response of extruded geogrids with good accuracy, and accounting for softening and fracture responses.

1. Introduction

Geogrid reinforcements have been used extensively in many geotechnical structures (e.g. foundations, pavements, embankments, retaining walls) improving their performance and durability while being cost-competitive against traditional geotechnical solutions [1]. In these applications, the geogrid increases the strength of the structure as soil loads are transferred to reinforcement by means of its tensile strength. Thus, tensile load–strain response is a crucial property of geogrids and other geosynthetics used in reinforcement [2,3].

The tensile load response of polymeric materials, such as geogrids, exhibits strain rate dependency and nonlinear stiffness, particularly for those manufactured from polypropylene and high-density polyethylene (HDPE and PP). The strain-rate influence on the load–strain behaviour of these materials is well documented [4,5]. The markedly nonlinear stiffness of polymeric materials is a function of their morphology and local crystallinity of polymeric chains that can also account for changes in the tensile response along the length of the specimen [6].

Historically, the design of reinforced soil structures uses limit equilibrium methods and includes simplifications related to the geometry and properties of reinforcements considered in the design. More recently, numerical modelling has become more common in the design, particularly for complex geometries, construction sequences or geological and geotechnical conditions. For example,

---

[*] Corresponding author.
E-mail addresses: lucaspaiva@ua.pt (L. Paiva), mlopes@ua.pt (M. Pinho-Lopes), robertt@ua.pt (R. Valente), mpaula@ipb.pt (A.M. Paula).

https://doi.org/10.1016/j.finel.2023.104008
Received 27 March 2023; Received in revised form 20 July 2023; Accepted 20 July 2023

Available online 9 August 2023
0168-874X/© 2023 The Author(s). Published by Elsevier B.V. This is an open access article under the CC BY license (http://creativecommons.org/licenses/by/4.0/).

numerical modelling using the Finite Element Method (FEM) can be considered the new industry standard for geotechnical design, being a powerful tool that can tackle both complex geometries and nonlinear material properties. A number of studies have shown that 3D FEM can be used to predict ultimate [7,8], and service limits [9–11], being also useful for parametric analysis [12,13] in a variety of geogrid-reinforced structures. The majority of papers do not detail the specifics of the geogrid geometry or its constitutive models in favour of a more generalized understanding of the reinforcement effect. Therefore, the objective of the present paper is to explore in depth 3D models of in-isolation response geogrids under uniaxial tensile loading, considering their detailed geometry combined with nonlinear constitutive models, and grounded in experimental data. This is achieved in two phases: (I) a benchmark exercise to calibrate the FEM model using literature data; (II) case study using the calibrated model, consisting of the tensile response of three geogrids in order to validate and explore the capabilities of the model.

2. Background

2.1. 3D geometry of in-isolation tensile response

In the literature there are still few studies focusing on the full 3D modelling of geogrids and their real geometry. Hussein and Meguid [14] presented a 3D model to simulate the tensile response of a biaxial geogrid using solid finite elements and nonlinear elastic–plastic properties. The model required the Young's modulus and plastic strain curves of the geogrid. Anisotropy was not considered directly, but instead was taken as the average between the tensile response along two orthogonal directions. Nevertheless, the model was able to simulate the experimental tensile response of the geogrid adequately. A comparison was also made between the detailed 3D geometry and an equivalent 2D plane sheet. In order to produce the same response, the plane (continuous) shell required extensive calibration to compensate the additional stiffness inherent to the 2D model, since apertures made 70% of the total area of the studied geogrid [14]. Hence, if geometric simplifications are required (e.g., to reduce computational time), the 3D model proved to be an useful first step in the modelling process, validating the material properties that can be than used in 2D models, given an adjustment in the shell/membrane thickness.

Amirhosseini et al. [15] studied the tensile response of a HDPE biaxial geogrid, exploring alternative models to deal with the difference in thickness between the junctions and the ribs that composed the geogrid. Three models were proposed: Model 1 used the exact geometry (i.e. with minimum simplifications in geometry) including the actual thickness of junctions and ribs; Model 2 considered a constant thickness, equal to cross rib thickness throughout the grid, while defining a higher stiffness for the junction to compensate for the thickness reduction; Model 3 also considered a constant thickness equal to that of the cross rib, but did not account for any compensation in stiffness. Experimental results were available only for the weak direction, where all three models were in agreement with each other and with the experimental results. For the strong direction, deviations between the three models became noticeable, but no experimental data was presented by Amirhosseini et al. [15]. From a strain distribution perspective, Models 1 and 2 produced similar results (points a and b in Fig. 1), while Model 3 developed strains in the longitudinal ribs (point c Fig. 1) that are unlikely to occur. Hence, for this geogrid thickness was a governing geometric feature that should be properly captured by the model or adjusted via equivalent material properties.

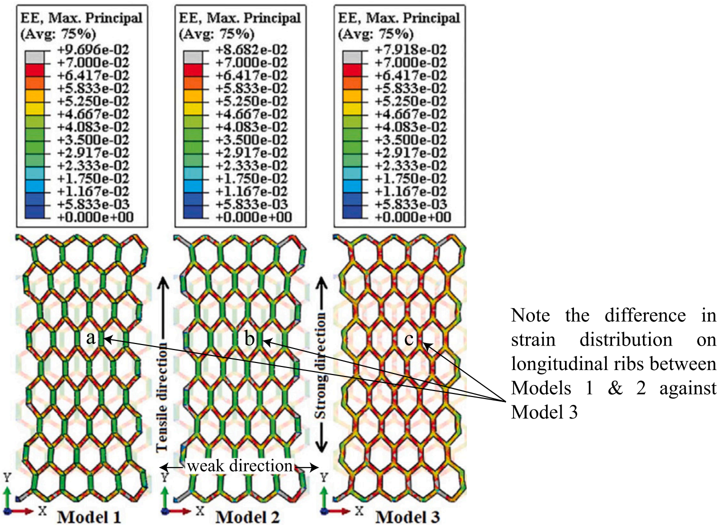

Note the difference in strain distribution on longitudinal ribs between Models 1 & 2 against Model 3

Fig. 1. Elastic strain distributions for the three models: (a) Model 1; (b) Model 2; (c) Model 3. [15].

2.2. Nonlinear constitutive models for tensile response

Two typical load–strain responses of geosynthetics, as presented by Liu and Ling [16], are shown in Fig. 2 (Type A and B). These responses are usually represented by rheological or mathematical models. Rheological models [17,18] combine a series of springs

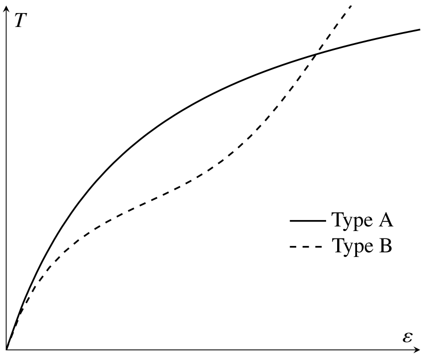

Fig. 2. Nonlinear load–strain relationships of geosynthetics: Type A and Type B [16].

and dashpots to characterize the viscoelastic and viscoplastic response of polymers with reasonable accuracy. However, rheological models often do not account for the macrostructure effect and are not optimized for parametric analysis, being not particularly suited for the FEA (finite element analysis) purposes herein reported.

A second class of models are mathematical models. These models are phenomenological, i.e., they mathematically represent the experimental data. In this approach, geosynthetics are represented as homogeneous and, often, isotropic materials. It is important to note that the thickness of geosynthetics is not constant and, in real applications, it varies with the confining pressure from the surrounding soil. Because of that, the tensile response of geosynthetics is represented using a force per unit width, instead of a stress. The main mathematical models reported in the literature are polynomial (Eq. (1)) and hyperbolic functions (Eq. (2) and (3)) [19]. As reported by Lombardi et al. [20], although high order polynomial functions (up to order 6) can fit well the experimental data for both A and B types of response, their coefficients have no physical meaning. Hyperbolic models can be sufficiently accurate, accounting for model parameters that can be related to the tensile properties of geosynthetics (Eq. (4) and (5)).

$$T_n = \sum_{i=1}^{n} a_i \cdot \varepsilon^i, \tag{1}$$

$$T_A = \frac{\varepsilon}{a + b \cdot \varepsilon}, \tag{2}$$

$$T_B = \frac{\varepsilon}{a + 2b \cdot \varepsilon} + \frac{e^{-\alpha(\varepsilon - \varepsilon_{\max})^2}}{2b}, \tag{3}$$

$$J_i = \frac{1}{a} \quad \varepsilon \to 0, \tag{4}$$

$$T_{\max} = \frac{1}{b} \quad \varepsilon \to \varepsilon_{\max}. \tag{5}$$

In the previous equations: T_n, T_A, T_B are the tensile forces per unit width for polynomial, hyperbolic type A and hyperbolic type B models respectively; n is the order of the polynomial model, a_i are the parameters of the polynomial model; a, b, α are the parameters of the hyperbolic models; J_i is the initial stiffness; and $T_{\max}$ is the ultimate tensile strength. In the next section, proper numerical treatment will be presented to generalize the load per unit width into three-dimensional models.

3. Materials and methods

3.1. Methods

The 3D modelling of the in-isolation tensile tests of this study was achieved in two phases:

(I) Benchmarking of experimental results presented by Hussein and Meguid [14],
(II) Case study for three geogrids using the calibrated model from the benchmarking exercise.

3.2. Benchmarking

Traditional general-purpose Finite Element (FE) packages require, besides material properties and geometry, a considerable number of parameters to be set. To further evaluate the influence of these parameters, in-isolation experimental data from [14] for a biaxial extruded geogrid and on the cross machine (XMD) direction was used. The model selected for the benchmark test had the same geometry, constraints and material properties defined by Hussein and Meguid [14]. Aspects related to the element shape and integration function, mesh and stabilization were studied to find the optimal setup for the 3D simulation of the in-isolation tensile response of geogrids. Hussein and Meguid [14] reported data from uniaxial tests along both the machine and the cross-machine directions of the geogrid. Then, in their numerical models, Hussein and Meguid [14] used an average of these two responses. In this paper a similar approach was used for this benchmarking exercise.

A series of 18 simulations were performed to assess the influence of simulation parameters in the simulation of the tensile response, being listed in Table 1 (X for performed tests). The indicated test names follow a logical rule, with the name of the ABAQUS element [21] at the beginning, followed by the mesh size in terms of rib thickness, and a final letter S to indicate whether stabilization was used. For example, a test name C3D8R_2t_S indicates that the C3D8 hexaedric element was used, along with a mesh equal to two times the rib thickness and with stabilization activated.

Table 1
Benchmarking test table.

Test name	Element shape[a]	Mesh	No stabilization	With stabilization
C3D4_t	tet	t	X	X
C3D4_2t	tet	2t	X	X
C3D4_3t	tet	3t	X	X
C3D8_t	hex	t	X	X
C3D8_2t	hex	2t	X	X
C3D8_3t	hex	3t	X	X
C3D8I_t	hex	t		X
C3D8I_2t	hex	2t		X
C3D8I_3t	hex	3t		X
C3D8R_t	hex	t		X
C3D8R_2t	hex	2t		X
C3D8R_3t	hex	3t		X

[a] hex being 8-node hexahedrons and tet being 4-node tetrahedrons.

3.3. Stabilization

In the context of FEM analysis for nonlinear problems, the convergence of equilibrium required for any node on a body is a function of internal forces I and external forces P:

$$P - I = 0. \tag{6}$$

The nonlinear displacement response to a small load increment, ΔP, is calculated in Abaqus/Standard using the tangent stiffness, K_0, from the initial configuration u_0, illustrated in Fig. 3.

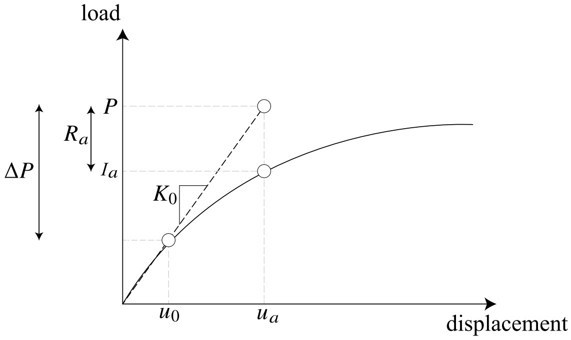

Fig. 3. Iteration of convergence [21].

The displacement of the new structure, denoted as u_a, associated with the updated internal energy, I_a, is calculated based on ΔP. Notably, in nonlinear problems, the residual force, R_a, will be larger than 0:

$$R_a = P - I_a. \tag{7}$$

When the residual force is larger than the threshold defined for convergence (with the default value in Abaqus/Standard being 0.5% of the average external force P), convergence is not achieved.

Automatic stabilization is a technique that can be used in the solution of quasi-static nonlinear problems to deal with numerical instabilities that can arise. These instabilities are often due to the nonlinear nature of the problem, such as geometric or material non-linearities. The automatic stabilization in Abaqus/Standard is achieved by adding a damping force to the system, which acts to resist motion and stabilize the numerical solution. This is mathematically represented as viscous force, F_v, defined as follows:

$$F_v = c \cdot M^* \cdot v, \tag{8}$$

where c is the damping factor, M^* is an artificial mass matrix of unity density, $v = \Delta u/\Delta t$ is the vector of nodal velocities for the time increment Δt.

The balanced equilibrium is then defined as:

$$P - I - F_v = 0. \tag{9}$$

The automatic stabilization scheme in Abaqus/Standard often mitigates instabilities, but the damping factor may not always be optimal. If convergence issues arise, or if the solution is distorted, the damping factor may need adjustment. This could involve reanalysis with a larger factor and a post-analysis comparison of the dissipated and total strain energies [21]. Ultimately, finding the optimal damping factor requires iterative adjustment until a satisfactory solution is achieved. Thus, to verify the suitability of the chosen damping factor, the stabilized curves were compared with their respective non-stabilized pairs.

3.4. Case study

The case study was composed of four steps:

(i) Three geogrids of different structure and materials were previously submitted to tensile tests along the XMD direction the according to BS ISO 10319:2015 [22], as presented by Pinho-Lopes et al. [23], Pinho-Lopes and Lopes [24].
(ii) A data-driven procedure was developed to evaluate a single best overall representative load–strain curve from the five specimens of each geogrid tested along the MD direction.
(iii) Hyperbolic models were applied to the experimental results in order to capture the nonlinear tensile response of the geogrids. Elastic and plastic parameters were evaluated according to the hyperbolic models.
(iv) Combining the experimental and the benchmark results, a numerical model was developed to simulate the tensile test, incorporating the 3D geometric features and the constitutive models fitted to the experimental data.

3.4.1. Geogrids studied

Three extruded geogrids were considered: GG1 and GG2, biaxial and polypropylene (PP); GG3, uniaxial and high-density polyethylene (HDPE), Fig. 4. The main nominal properties of the geogrids included in the product data sheet are summarized in Table 2.

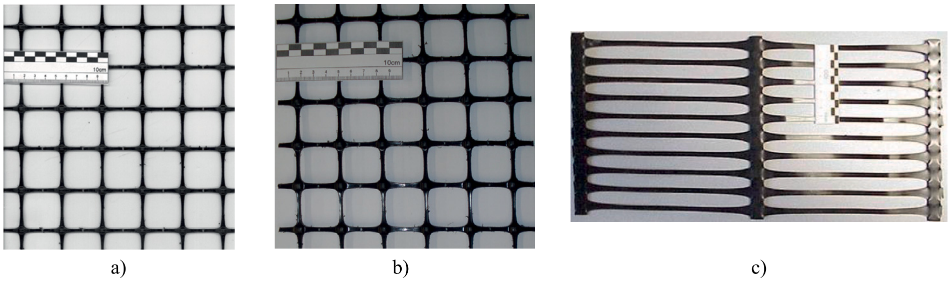
a)	b)	c)

Fig. 4. Geogrids studied: (a) GG1, [23]; (b) GG2, [23]; (c) GG3, [24].

Table 2
Nominal properties of the geogrids.

Geogrid			GG1	GG2	GG3
Constituent polymer			PP	PP	HDPE
Ultimate tensile strength[a]	T_{nom}	kN/m	20	40	68
Strain at maximum load[a]	ε_{nom}	%	10	10	11
Thickness of longitudinal rib	t_{LR}	mm	1.1	2.2	0.9
Thickness of junction	t_J	mm	4.1	5.8	2.6

[a] According to BS ISO 10319.

3.4.2. Wide-width tensile tests

The three geogrids had been previously submitted to wide-width tensile tests performed according to BS ISO 10319:2015 [22] in the machine direction (MD). Data for 5 specimens of each geogrid were available, obtained using a 250 kN universal testing machine under a constant strain rate of 20%/min. A video-extensometer was used to measure the deformation within a reference length of 60 mm, as defined by BS ISO 10319:2015 [22].

3.4.3. Data-driven model

Variability between individual specimens is a common phenomenon in materials testing, attributable to the intrinsic properties of the materials, manufacturing processes, and variations in testing conditions. This often leads to unique load–strain responses for each specimen. Although BS ISO 10319:2015 [22] mentions the conditions in which specimen results shall be discarded, selecting a single "best" load–strain curve as representative may not effectively capture this inherent variability.

To find a suitable representative load–strain curve from each set of results from the 5 specimens, a data-driven model was developed using Python. Initially, the load–strain curve of each specimen was converted into a strictly-increasing series. That was achieved by removing duplicates or out-of-order strain data. Then, a Piecewise Interpolating Polynomial (PCHIP) [25] was applied to the data of each specimen within the strain domain, i.e., from 0% to the corresponding strain for the maximum tensile force recorded. The purpose of converting the discrete experimental data into an interpolation function is to make it possible to evaluate the mean, since each specimen curve has a different domain (strain data). Another advantage of using interpolation functions is the possibility to perform resampling. Load–strain curves can have thousands of points, and a PCHIP function allows for the control of the number of points by setting a custom domain.

3.4.4. Hyperbolic-based constitutive models

The three geogrids studied followed a type A response. The mean results from the data-driven model developed were fitted with the type A hyperbolic model (Eq. (2)) using Python Scipy library [26]. Two statistical parameters, i.e., coefficient of determination (R^2) and root-mean-square deviation (RMSE) were used to access the goodness of fit.

3.4.5. FEM models

3D FEM tests were performed combining the explicit geometry and the hyperbolic constitutive models previously discussed. All simulations were performed using ABAQUS/Standard solution option. Three-dimensional geometric details were directly imported from AutoCAD including the thickness profiles for each geogrid, and the same physical test boundary conditions were applied. Elastic and plastic properties were derived from the hyperbolic models.

3.4.6. Geometry and boundary conditions

The geometry of the two biaxial geogrids (GG1 and GG2) and the uniaxial geogrid (GG3) were created in ABAQUS as a 3D part, with the dimensions shown in Fig. 5. The numerical tensile test was carried out by restraining the left end along the longitudinal and transversal (XY) directions and by applying the same strain rate of 20%/min used in the experimental tests at the right end of each numerical specimen of geogrid. Only half of the longitudinal ribs were modelled by means of a XZ symmetry constraint, as shown in Fig. 6.

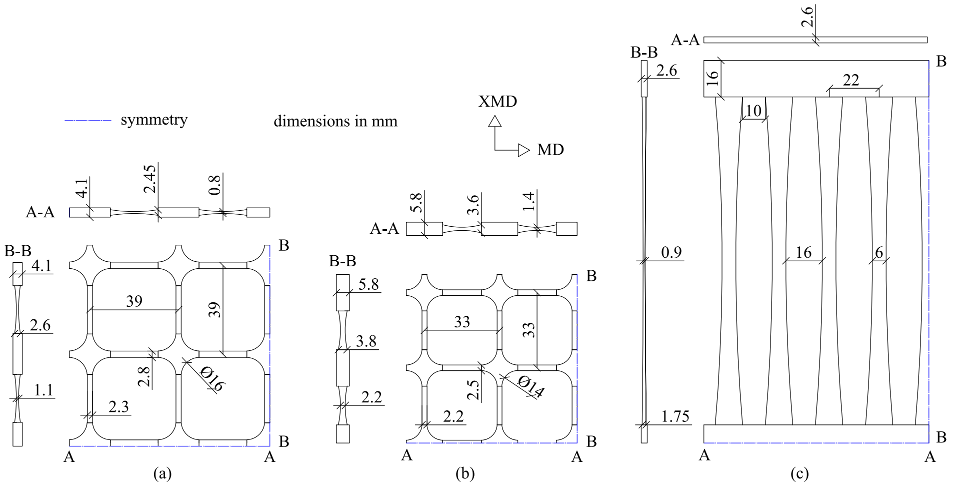

Fig. 5. Adopted geometry of the three geogrids studied: (a) GG1; (b) GG2; (c) GG3.

3.4.7. Elastic–plastic model

Hyperelastic and nonlinear elastic models (*e.g.*, elastic–plastic models) are commonly associated with polymeric materials such as rubbers, that are known for their ability to sustain deformation and return to their original shape when load is removed. This suggests a nonlinear yet reversible relationship between stress and strain in these materials. However, despite being polymers, HDPE and PP usually do not display this level of pronounced elastic response [4,16,27]. Moreover, purely elastic models do not account for hardening or softening behaviour, as these responses occur after yielding. Thus, to properly account for these effects, an elastic–plastic model was chosen to represent the geogrids herein.

The constitutive models and data-driven frameworks previously discussed were established with reference to nominal (engineering) stresses and strains under one-dimensional conditions. To allow for an interpretation compatible with ABAQUS, the subsequent

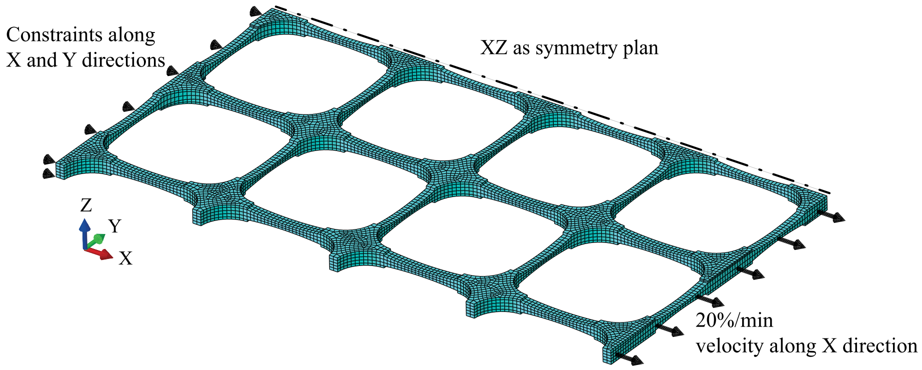

Fig. 6. Example of geometry and boundary conditions for GG1.

steps are required first to transform the nominal data into true 3D stresses and strains, and second, to break down the strain profile (Eq. (1) to (5)) into separate elastic and plastic components:

1. Convert nominal to true values of strains (Eq. (10)) and stresses (Eq. (11)):

$$\varepsilon_{true} = \ln\left(1 + \varepsilon_{nom}\right), \tag{10}$$

$$\sigma_{true} = \sigma_{nom}\left(1 + \varepsilon_{nom}\right), \tag{11}$$

2. Decompose strain data into elastic (Eq. (12)) and plastic (Eq. (13)) strains:

$$\varepsilon^{el}_{true} = \frac{\sigma_{true}}{E}, \tag{12}$$

$$\varepsilon^{pl}_{true} = \varepsilon_{true} - \varepsilon^{el}_{true}, \tag{13}$$

where ε_{true} is the true strain; ε_{nom} is the nominal strain; σ_{true} is the true stress; σ_{nom} is the nominal stress; ε^{pl}_{true} is the true plastic strain; ε^{el}_{true} is the true elastic strain; and E is the Young's modulus.

The Young's modulus was taken as the initial stiffness considering the initial stiffness per unit of width, Eq. (4). The Poisson's ratio was taken as 0.3 [14]. As the experimental tensile data suggested, the elastic zone for the geogrids studied is small, being assumed to be valid until the 1% limit of the maximum load for all geogrids. The remaining strain profile is taken as plastic, with plastic strains obtained by subtracting the elastic component from the full strain data, Eqs. (12) and (13). More details on this decomposition can be found in [21].

3. Three-dimensional generalization:

In 3D continuum mechanics, a stress tensor, labelled as σ_{ij} $(i, j = x, y, z$, is composed of nine components, which dictate the stress state of a material's point or element under a certain load [28]. The hydrostatic, or mean stress (σ_m), also known as equivalent stress, is given by:

$$\sigma_m = \frac{1}{3}\left(\sigma_1 + \sigma_2 + \sigma_3\right), \tag{14}$$

where σ_1, σ_2 and σ_3 represent the principal stresses. The deviatoric stress tensor, denoted as S_{ij}, is computed as the difference between the original stress tensor (σ_{ij}) and the hydrostatic stress, multiplied by the unit tensor ($\sigma_m\delta_{ij}$), that is:

$$S_{ij} = \sigma_{ij} - \sigma_m\delta_{ij}. \tag{15}$$

Similarly, the deviatoric strain tensor (e_{ij}) is the difference between the strain tensor (ε_{ij}) and the mean strain ($\varepsilon_m\delta_{ij}$), expressed as:

$$\varepsilon_m = \frac{1}{3}\left(\varepsilon_{xx} + \varepsilon_{yy} + \varepsilon_{zz}\right), \tag{16}$$

$$e_{ij} = \varepsilon_{ij} - \frac{1}{3}\varepsilon_{kk}\delta_{ij} = \varepsilon_{ij} - \varepsilon_m\delta_{ij}, \tag{17}$$

where ε_m is the mean strain and ε_{kk} is the volumetric strain. For materials that are homogeneous and isotropic, the elastic stress tensor is dictated by two Lamé constants [29], λ (bulk modulus) and μ (shear modulus). These material-specific quantities emerge in stress–strain relations. Utilizing these Lamé constants, the stress tensor can be represented as:

$$\sigma_{ij} = 2\mu\varepsilon_{ij} + \lambda\varepsilon_{kk}\delta_{ij}. \tag{18}$$

For linear isotropic materials, Lamé constants can be directly written in terms of the Young's modulus E and Poisson's ratio ν:

$$\mu = G = \frac{E}{2(1+\nu)}, \tag{19}$$

$$\lambda = \frac{E\nu}{(1+\nu)(1-2\nu)}. \tag{20}$$

Strain decomposition: The deformation rate is the summation of the elastic $\left(\dot{\varepsilon}_{ij}^{el}\right)$ and plastic $\left(\dot{\varepsilon}_{ij}^{pl}\right)$ strain rate components:

$$\dot{\varepsilon}_{ij} = \dot{\varepsilon}_{ij}^{el} + \dot{\varepsilon}_{ij}^{pl}. \tag{21}$$

Yield condition: Numerical models of plasticity must differentiate between elastic and plastic responses. Thus, a framework is needed to outline (a) the yield surface, where yielding takes place; (b) the flow rule, dictating the direction of plastic deformation; and (c) the hardening law, which outlines how flow changes with plastic deformation. Therefore, the yield surface is defined by a function of the specified form:

$$f\left(\sigma_{ij}, \dot{\varepsilon}_{ij}^{pl}, T, k^n\right) = 0, \tag{22}$$

Associated flow rule: where the yield surface is a function of the stress tensor (σ_{ij}), plastic strain rate $\left(\dot{\varepsilon}_{ij}^{pl}\right)$, temperature ($T$) and a hardening parameter (k^n). When the function's value falls below or equals zero ($f \leq 0$), this denotes that the material is within the range of elastic deformation. Conversely, in scenarios of rate-dependent plasticity, the function's value exceeds zero ($f > 0$), which implies the presence of stress states that surpass the yield surface [21,28].

If the model is assumed to be under temperature-independent conditions, elasticity can be directly written in terms of the volumetric and deviatoric components:

$$\sigma_m = K\varepsilon_{kk}, \tag{23}$$

$$S_{ij} = \sigma_{ij} - \sigma_m \mathbf{I}, \tag{24}$$

where $\mathbf{I}$ is the identity tensor. Eqs. (23) and (24) are equivalent of Eqs. (17) and (18). Employing the von Mises yield function implies that no volumetric plastic strains will occur; given the high elastic modulus, any volume alteration will be minimal. The associated flow rule follows the normality condition, defined as:

$$de_{ij}^{pl} = d\dot{e}_{ij}^{pl} \cdot \frac{3}{2}\frac{S_{ij}}{q}, \tag{25}$$

where q is the effective von Mises stress:

$$q = \sqrt{\frac{3}{2} S : S}. \tag{26}$$

Combining Eqs. (26) and (22), the von Mises failure criterion can be written in terms of the second deviatoric stress invariant:

$$f(J_2) = 0 \quad \text{or} \quad \sigma_y - \sqrt{\tfrac{3}{2} S : S} = 0, \tag{27}$$

where σ_y is the yield stress of the last increment. Similarly, the strain from the deviatoric strain, or equivalent strain, is expressed as:

$$\varepsilon_{eq} = \sqrt{\frac{2}{3}(e_{ij} e_{ji})}. \tag{28}$$

Alternatively, (27) and (28) can be written in terms of principal stresses and strains, under plane stress conditions, sketched in Fig. 7:

$$f(\sigma_y) = \sqrt{\frac{1}{\sqrt{2}}\left[\left(\sigma_1 - \sigma_2\right)^2 + \left(\sigma_1 - \sigma_3\right)^2 + \left(\sigma_2 - \sigma_3\right)^2\right]}, \tag{29}$$

$$\varepsilon_{eq} = \sqrt{\frac{\sqrt{2}}{3}\left[\left(\varepsilon_1 - \varepsilon_2\right)^2 + \left(\varepsilon_1 - \varepsilon_3\right)^2 + \left(\varepsilon_2 - \varepsilon_3\right)^2\right]}. \tag{30}$$

The material's behaviour is described by Eqs. (14) through (30). In any given increment where plastic flow is taking place (evaluated by calculating S_{ij} under the elastic regime, *i.e.*, $f > 0$), it is necessary to integrate and solve these equations to determine the state at the end of that increment). Moreover, an isotropic hardening is assumed, *i.e.*, the yield surface changes size uniformly in all directions such that the yield stress increases (or decreases) in all stress directions as plastic straining occurs. While the term "hardening" is commonly used to refer to this model, it is important to note that it can encompass both strain hardening and softening, or a sequential process of hardening followed by softening. This will be discussed in the following.

4. Damage evolution:

To model the rupture of ribs that reach full plasticity and allow the mesh element removal, a ductile damage parameter was defined. For elasto-plastic materials at maximum plasticity, the following damage response is seen in two forms: softening and degradation of the elasticity. In Fig. 8a, the dashed line represents the stress–strain response without a damage criterion (softening), while the solid line shows a damaged response (fracture). For the purposes of modelling the tensile response under ultimate limits, a simplified model was adopted, namely, a fracture model considering that no plastic strains are developed after the damage is started, i.e., the rupture strength being equal to the ultimate strength, Fig. 8b.

In ABAQUS, the damaged response is achieved by providing two parameters: the plastic strain at damage initiation and the damage evolution law. The plastic strain at damage initiation can be calculated by:

$$\varepsilon_0^{pl} = \varepsilon_0 - \frac{\sigma_0}{E}, \tag{31}$$

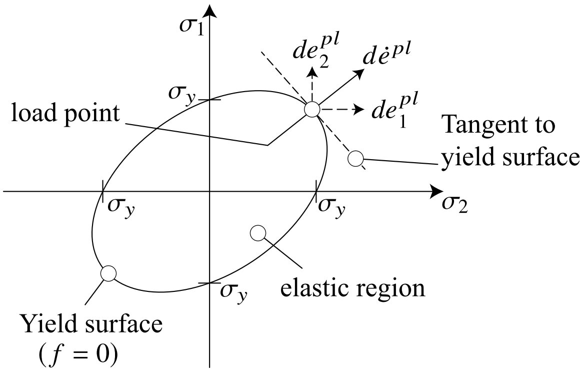

Fig. 7. von Mises plasticity surface under plane stress, with the plastic increment $d\dot{e}^{pl}$ in the normal direction tangent to the yield surface [30].

where σ_0 is the yield stress; ε_0 is the equivalent plastic strain at yield; E is the Young's modulus.

The damage evolution law is defined in such way that the solution accounts for the mesh influence. When damage occurs, the validity of the stress–strain curve to properly represent the material is lost, due to strain localization [31]. To alleviate this influence, the displacement at damage will include a mesh proportionality factor. Hence, the effective plastic displacement is defined by an evolution equation, as:

$$u^{pl} = L \cdot \varepsilon_0^{pl}, \tag{32}$$

where u^{pl} is the effective plastic displacement; L is the characteristic length of element. This length is based on the mesh element type, being taken for 3D elements is taken as the length across the largest face area. This law also assumes a linear damage evolution until fracture, as seen in Fig. 8b:

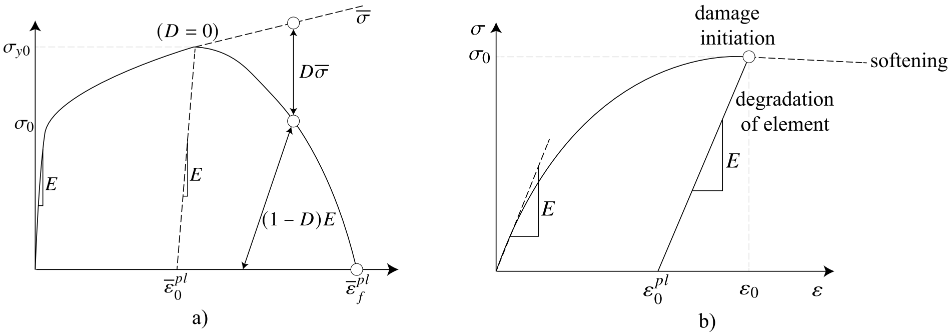

Fig. 8. Damage model: (a) Stress–strain curve with progressive damage degradation as available in [21]; (b) Adopted modified damage evolution curve.

The calibration of the yield pair $(\sigma_0, \varepsilon_0)$ requires a first run with the model without the damage initiation, recording the yield stress at the point where plasticity is maximum, *i.e.*, when the equivalent plastic strain ε_{eq}, Eq. (28), reaches the unity.

A flowchart summarizing the previously described procedure is shown in Fig. 9. Since plastic parameters were provided, the default strain output by ABAQUS was the logarithmic strain. From this formulation, all the outputs from the simulations are in terms of true stresses and strains. To compare the experimental data with simulation results, Eqs. (10) and (11) were used to display simulation results in terms of the nominal values.

All geogrids were simulated in ABAQUS in two runs: (i) with the regular elasto-plastic model, and (ii) with the damage evolution option. Table 3 summarizes the modelling parameters for the three geogrids studied.

Table 3
Modelling parameters for case study simulations.

Geogrid	Mesh element	Mesh size [mm]	N nodes	Wallclock [mm:s]	Stabilization
GG1	C3D8R	0.5	28370	01:09	Yes
GG2	C3D8R	1.1	46337	05:14	Yes
GG3	C3D8R	0.9	8018	03:22	Yes

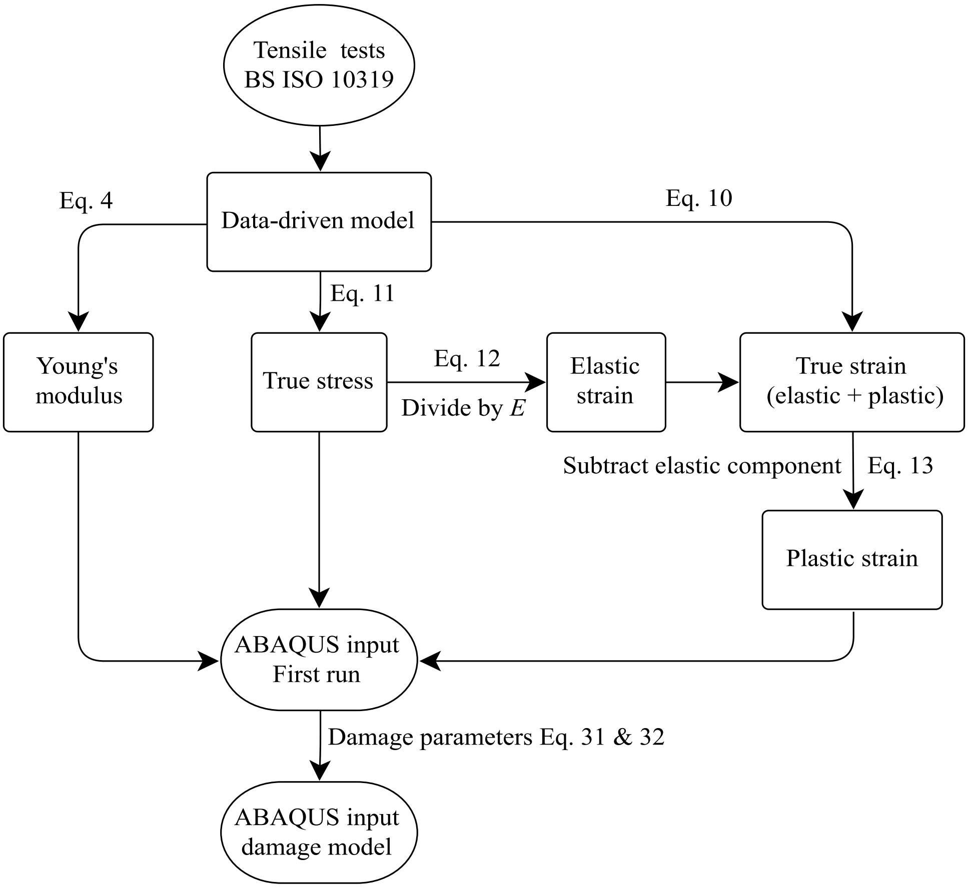

Fig. 9. Flowchart for generating required ABAQUS input.

4. Results

4.1. Benchmark results

For 3D solid geometries, two element shapes are available in Abaqus: 8-node hexahedrons (hex) and 4-node tetrahedrons (tet). Tet elements can fit complex geometry better at the expense of adding more elements to the same mesh. For the geogrids studied, the junction nodes with curved profile required either tet elements or an extra step before meshing where the zones were sufficiently sectioned to make a hex mesh generation possible. The results have shown (Fig. 10b) no effect in the stress and strain results, up to the point of maximum force, by the choice of tet or hex elements.

Three element types were tested: full integration (C3D8), reduced integration (C3D8R) and incompatible mode (C3D8I) elements. Full or reduced integration is a reference to the number of Gauss points used to perform the numerical integration, with full integration elements having 8 internal Gauss points and reduced integration elements having a single central Gauss point. Incompatible elements have the volumetric locking effect reduced, at the cost of 13 additional degrees of freedom than a regular full integration (to better capture bending behaviour). Since the geogrid tensile tests do not generate bending forces, the choice of element type showed no effect in the simulation results up to the maximum strain measured experimentally (Fig. 10b).

The influence of meshing was also studied. With the thickness of the geogrid elements being the governing geometric property under tensile test conditions, a parametric test showed (Fig. 10c) that a mesh size between t and $2t$ (t being the rib thickness) is sufficiently accurate while remaining computationally efficient. This finding is aligned to the mesh size suggestion given by [14]. Furthermore, to reduce the influence of the mesh in the results, all ribs of each numerical specimen were generated with the same mesh.

Due to necking effects produced in the thinnest zone of the rib during loading, numerical instability can arise. To prevent premature termination of the simulation due to this instability, a damping factor of 0.02% was used when needed (tests with stabilization, Table 1). This damping value is obtained by trial and error, and for the simulations herein reported, the selected damping factor was able to overcome premature termination of the simulation, without influencing the load–strain results (Fig. 10d).

An execution time benchmark is summarized in Table 4. Due to an average of 6 times more elements for the same mesh, tetrahedric shape elements were more costly than hex elements. Regarding these formulations, C3D8I elements showed the longest execution time, with C3D8R elements being the most time efficient, as expected.

Table 4
Benchmark time for element type and mesh options.

Mesh	N nodes		Wallclock [mm:s]			
	C3D4	C3D8[a]	C3D4	C3D8	C3D8I	C3D8R
t	14792	11352	27:20	10:11	37:29	07:35
$2t$	3587	3776	05:26	03:25	19:35	04:08
$3t$	1862	1890	01:18	00:53	04:04	0:37

[a] Number of nodes are the same for CD38, CD38I and C3D8R.

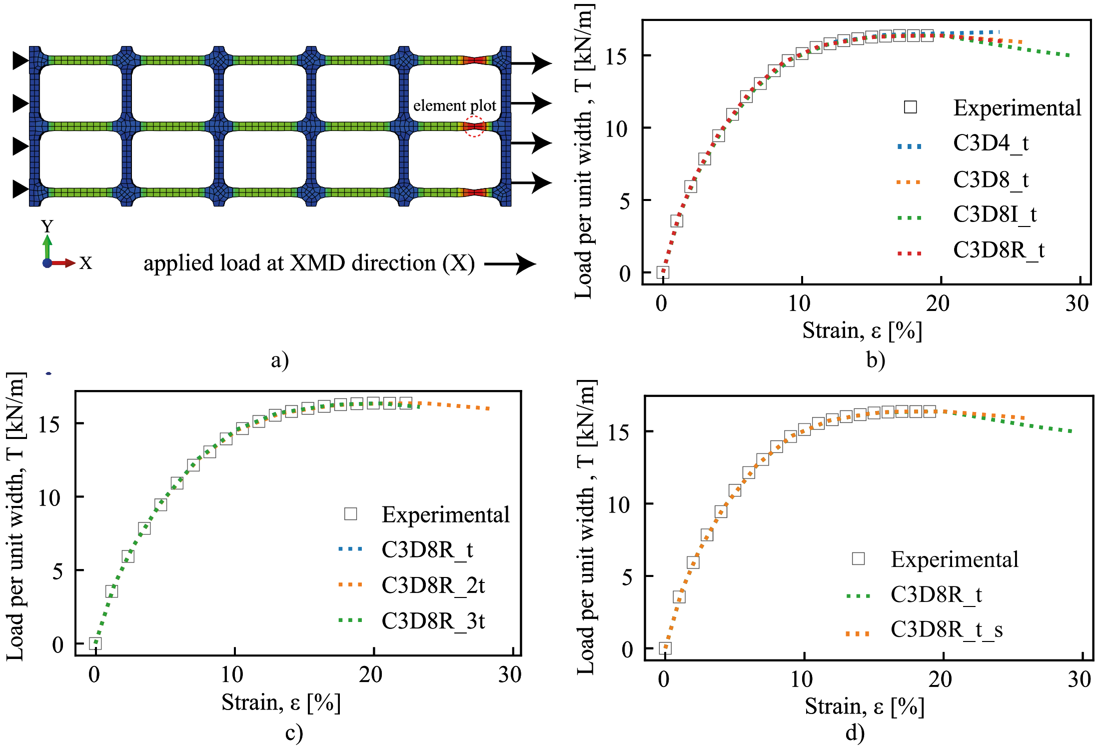

a) b) c) d)

Fig. 10. Effect of modelling options: (a) Geometry and constraint for XMD direction as used by Hussein and Meguid [14]; (b) Comparison of distinct element types; (c) Comparison of distinct meshes (t being the rib thickness); (d) Comparison of using (or not) a stabilization procedure.

This preliminary parametric study showed that C3D8R elements with a mesh similar to rib thickness values is a preferred setup in terms of trade-off between precision and time efficiency. Prior to full plasticity, there was no significant impact on the stress–strain curve by using full integration elements or finer meshes. However, after plasticity has onset, different element types lead to different softening curves (Fig. 10b) as no rupture law was defined. As the response of each geogrid was only analysed until the strain corresponding to failure, the response beyond that value of strain was not considered in the analysis.

4.2. Case study results

4.2.1. Data-driven model results

Fig. 11 and Table 5 summarize the load–strain response of 5 specimens for each geogrid obtained experimentally and the corresponding mean curve, obtained using the data-driven model. The mean curve for each set of 5 specimens proved to be the best representation of the overall response of each geogrid. The strain at maximum tensile force was also taken as the mean value for the 5 specimens. For the geogrids studied, a re-sampled data set with 50 points was deemed to be of enough precision to represent the load–strain curves (see Table 5). The data-driven model provided an average representation of all specimens. This statistically robust approach effectively mitigated the impact of outliers and variability was lower compared to any single specimen that could be taken as representative.

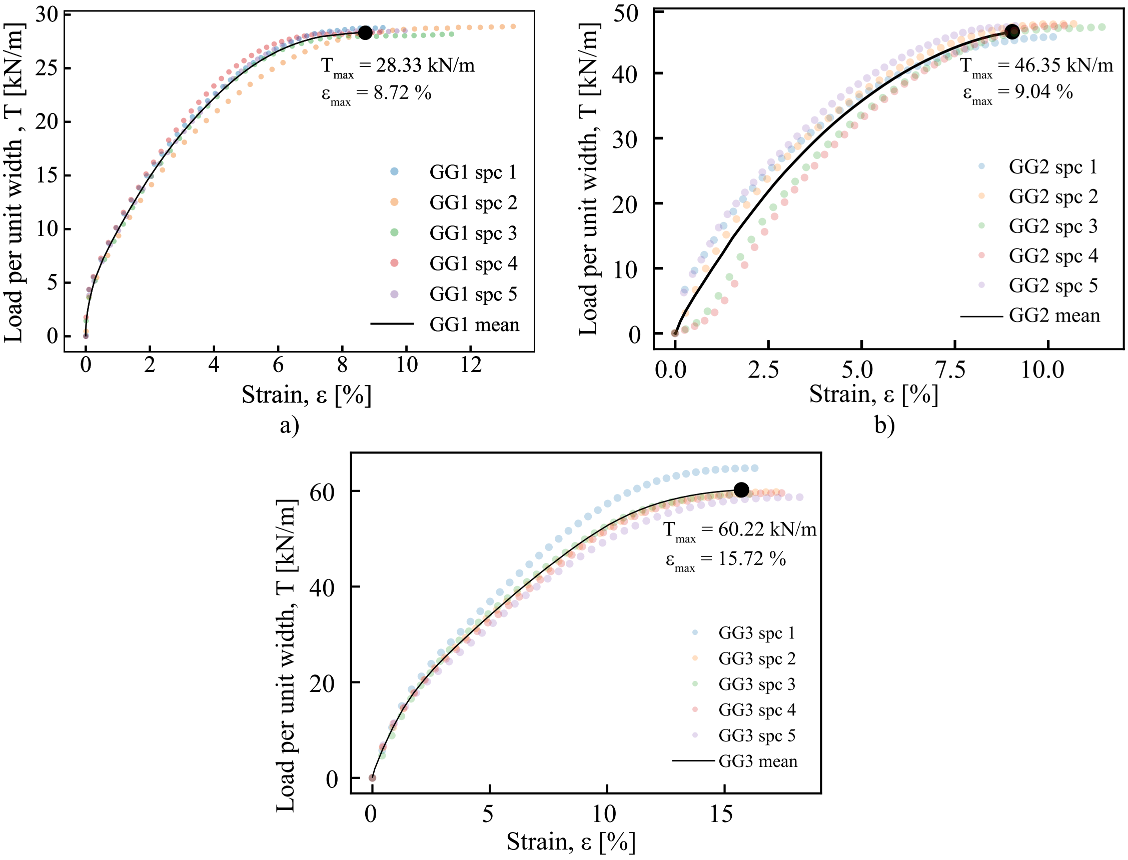

a)

b)

c)

Fig. 11. Experimental data from wide-width tensile tests, and the calculated mean values for the three geogrids: (a) GG1; (b) GG2; (c) GG3.

Table 5
Curve fitting results for the type A hyperbolic model, HA (Eq. (2)).

Geogrid	a	CV[a]	b	CV[a]	Ji[b] [kN/m]	R^2[c]	RMSE[d] [kN/m]
GG1	7.853E−02	2.321E−03	2.527E−02	4.457E−04	1270	0.978	1.093
GG2	8.397E−02	1.309E−03	1.163E−02	2.178E−04	1190	0.957	2.892
GG3	8.959E−02	1.722–03	1.042E−02	1.719E−04	1200	0.980	2.253

[a] Coefficient of variation.

[b] Initial stiffness calculated using Eq. (4).

[c] Average coefficient of determination between the hyperbolic model and the specimens.

[d] Average root-mean-square deviation between the hyperbolic model and the specimens.

The overlay plot between fitted hyperbolic models (HA fit) and experimental data (exp.) is shown in Fig. 12. The mathematical model showed a good fit against the experimental data, while slightly overestimating the ultimate tensile strength.

4.2.2. Response to tensile loading

The experimental and modelled load–strain curves for the three geogrids are compared in Fig. 13. Two reference points were selected to lay out the response at maximum plasticity: point (I) where the necking was observed; point (II) close to the centre of each specimen. The maximum load and respective strain for experimental and calculated models are given in Table 6. There was a good agreement between these experimental (physical test) and calculated (numerical test) results. The numerical tests led to an slight overestimate of the maximum tensile force of GG1 and GG3 (up to 3.5%) obtained experimentally, while for GG2 that force was underestimated by 0.3%. For GG2 and GG3, the strain for the maximum tensile force was overestimated in the numerical test (8.3% for GG2, and 0.8% for GG3); for GG1 the two results coincided. At point (I), strains were most pronounced, and after the full plasticity was reached, the simulation output exhibited softening. At point (II), the response up to before full plasticity was similar

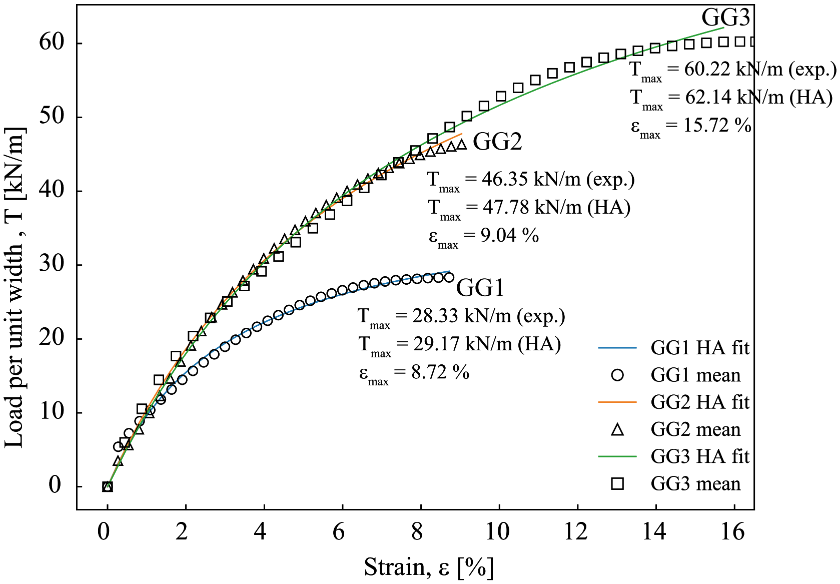

Fig. 12. Hyperbolic model fit for the three geogrids studied.

Table 6
Comparison between measured and calculated results for maximum load and strain.

Geogrid	Maximum load [kN/m]		Strain at maximum load [%]	
	Experimental	Calculated	Experimental	Calculated
GG1	28.33	29.20	8.72	8.72
GG2	47.78	47.65	9.04	9.79
GG3	60.28	62.45	15.99	16.11

to point (I). However, due to the strain concentration at point (I), the tensile load was released at point (II) and the other locations. The location of point (I) in the simulation is in line with the experiment results, where failure often occurs near the clamps.

The simulation test of GG3 showed residual strains slightly before the peak load at point (I), and the softening model at point (II) was able to simulate the post-plasticity response of the real test. For GG1 and GG2, the simulation results at point (II) also indicated a softening behaviour, but the measured data was followed by rupture. To better capture this response, the same model was adapted including the damage criterion described in Section 3.4.7, allowing for the immediate rupture and element deletion of mesh elements at the onset of plasticity.

The comparison between softening and fracture responses of GG1 is illustrated in Fig. 14. Since both models utilize the same stress–strain data prior plasticity, the stress distribution across the geogrid is the same (Figs. 14a and 14c). However, at the onset of plasticity the fracture curve was followed by the relaxation as seen close to the centre of the specimen.

The visual response of the fracture is a function of the simulation time. Fig. 14d shows that the fracture in fact happens almost instantly (*i.e.*, in all ribs) despite the initiation at the centre of the specimen. As discussed in Section 3.4.7, this model assumed that no plastic strain was developed after fracture along the whole geogrid. It is also worth noticing that for both softening and fracture models, the failure occurred on the same ribs close to the edge of the geogrid specimen where the displacement is applied.

5. Conclusions

Based on experimental data of wide-width tensile tests of geogrids, this study has furthered the understanding on the 3D numerical modelling of geogrids, incorporating hyperbolic constitutive models and damage/fracture models in ABAQUS. Firstly, a benchmarking setup was carried out to find the optimal simulation parameters and using literature data [14] as reference for calibration. Then, a case study was used to validate the described simulation methodology. For that, experimental data of in-isolation uniaxial tensile tests of three extruded geogrids were initially treated using PCHIP interpolation to find the most representative load–strain curve from the 5 specimens. Then, hyperbolic models were fitted to experimental data of each geogrid (representative curve generated using PCHIP interpolation). The constitutive models were combined with the 3D geometry, taking into account the different thickness of each part of the geogrids. From the comparison between experimental data and modelling results, the following main conclusions can be drawn:

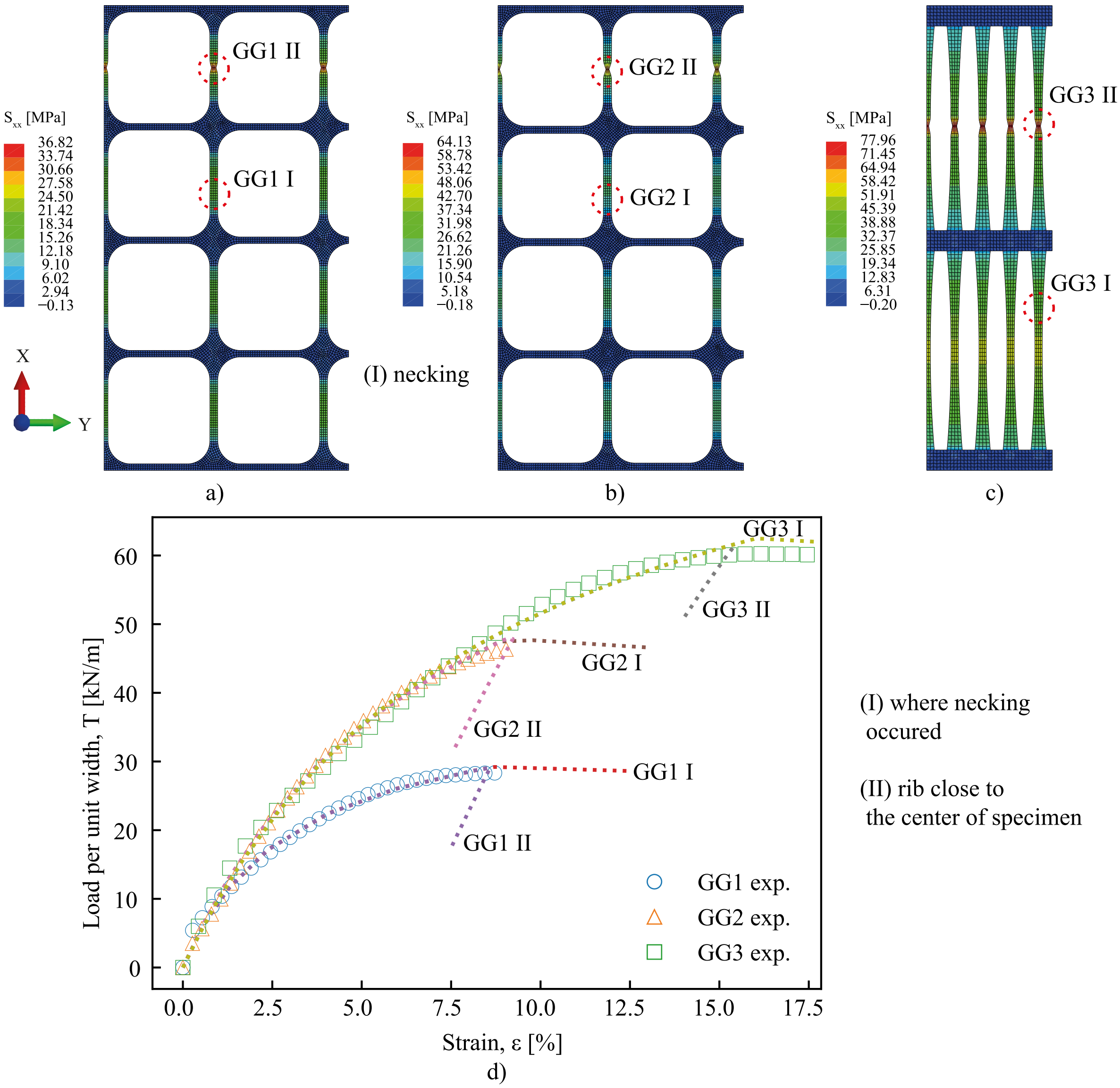

Fig. 13. Stress distribution on XX direction when maximum strength is reached: (a) GG1; (b) GG2; (c) GG3; (d) load per unit width/strain curves are in engineering values, and stress distributions are in true values.

- The PCHIP interpolation proved to be an useful framework for the data treatment of load–strain curves from wide-width tensile tests for several specimens. The interpolation exhibited a small coefficient of variation and low root-mean-square deviation. Moreover, the use of hyperbolic models and the correlation between its parameters with the nominal properties of the geogrids provided a practical way to evaluate the initial stiffness of the geogrids studied.
- The numerical models were in good agreement with the experimental tensile response, being able to capture initial stiffness, maximum tensile force and corresponding strain values. The location of maximum plasticity was also in accordance to the experimental results. The 3D models were capable of providing a better comprehension on the stress distributions within the various elements that compose the geogrids.
- The proposed methodology using ABAQUS allowed a flexible definition of the softening and fracture responses of the structures. For the softening option, the iterations after plasticity are by default assumed to be linear, and were able to capture the softening behaviour. The fracture option allowed the simulation of a sudden drop in tensile strength capacity at onset of plasticity. Although under linear assumptions, the two studied models provide a robust and replicable framework to simulate typical load–strain responses of geogrids with good accuracy.

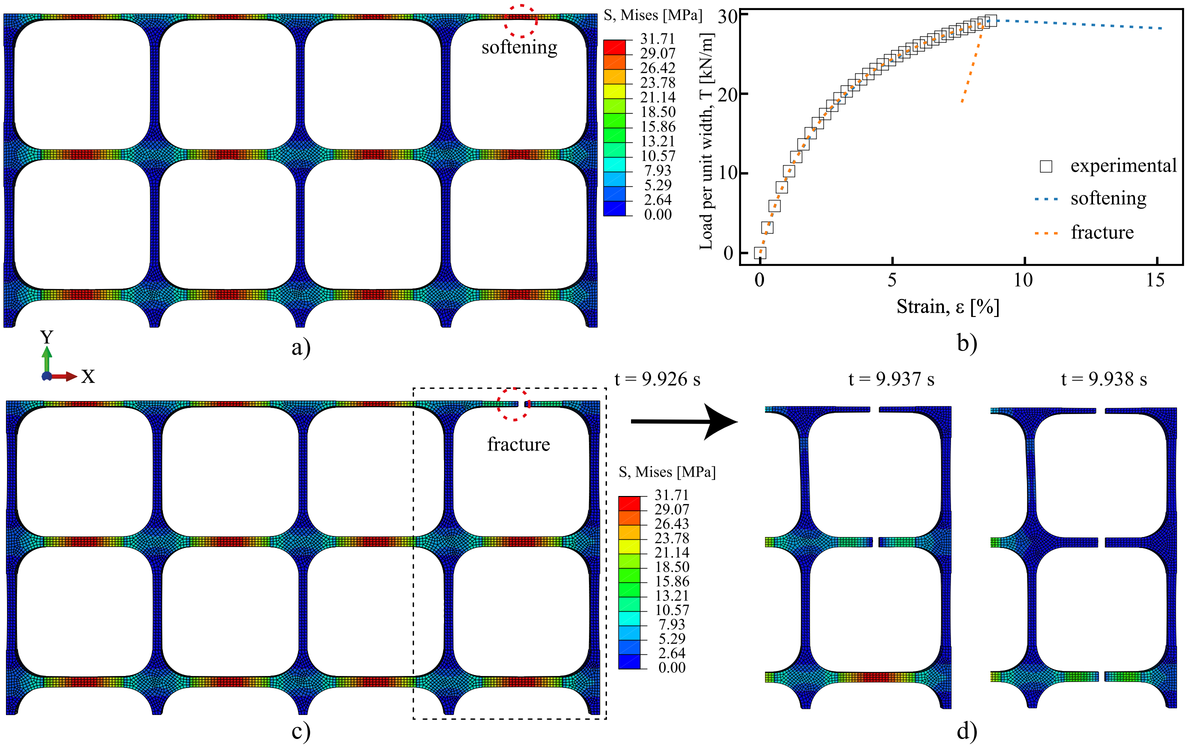

Fig. 14. Simulation results of fracture and softening for GG1: (a) von Mises stresses at maximum plasticity (softening); (b) Load per unit width/strain comparison for plot element; (c) von Mises stresses at maximum plasticity (fracture); (d) Evolution of fracture near the edge of the geogrid specimen where the load displacement is applied.

CRediT authorship contribution statement

Lucas Paiva: Data curation, Formal analysis, Funding acquisition, Investigation, Methodology, Validation, Writing – original draft, Writing – review & editing. **Margarida Pinho-Lopes:** Conceptualization, Data curation, Formal analysis, Funding acquisition, Investigation, Methodology, Project administration, Resources, Supervision, Validation, Writing – review & editing. **Robertt Valente:** Conceptualization, Formal analysis, Funding acquisition, Investigation, Methodology, Resources, Supervision, Validation, Writing – review & editing. **António Miguel Paula:** Conceptualization, Data curation, Formal analysis, Funding acquisition, Investigation, Methodology, Resources, Supervision, Validation, Writing – review & editing.

Declaration of competing interest

The authors declare the following financial interests/personal relationships which may be considered as potential competing interests: Lucas Paiva reports financial support was provided by Foundation for Science and Technology. Marnarida Pinho-Lopes reports financial support was provided by University of Aveiro Risks and Sustainability in Construction. Robert alente reports financial support was provided by University of Aveiro Centre for Mechanical Technology and Automation. Antonio Minuel Paula reports financial support was provided by University of Aveiro Risks and Sustainability in Construction.

Data availability

Research data available as a github repository.

Acknowledgements

The first author acknowledges the financial support by the Portuguese Foundation of Science and Technology — FCT under the MIT Portugal PhD Grant PRT/BD/153383/2021. The financial support of FCT is also gratefully acknowledged through the projects UIDB/04450/2020 (RISCO), UIDB/04708/2020 (CONSTRUCT), UIDB/00481/2020 (TEMA), UIDP/04450/2020 and CENTRO-01-0145-FEDER-022083 (CENTRO 2020).

Appendix A. Supplementary data

Supplementary material related to this article can be found online at https://doi.org/10.1016/j.finel.2023.104008. The ABAQUS models and the Python data-driven script related to this article can be found online at https://github.com/paiva96/Tensile-treatment.

References

[1] R.M. Koerner, Designing with Geosynthetics, Vol. 1, sixth ed., Xlibris Corporation, 2012.

[2] A. McGown, I. Yogarajah, K. Andrawes, M. Saad, Strain behaviour of polymeric geogrids subjected to sustained and repeated loading in air and in soil, Geosynth. Int. 2 (1) (1995) 341–355, http://dx.doi.org/10.1680/gein.2.0014.

[3] R.J. Bathurst, Challenges and recent progress in the analysis, design and modelling of geosynthetic reinforced soil walls, in: Proceedings of the 10th International Conference on Geosynthetics-Giroud Lecture, 21-25 September 2014, p. 38.

[4] A. Sawicki, K. Kazimierowicz-Frankowska, Influence of strain rate on the load-strain characteristics of geosynthetics, Geosynth. Int. 9 (1) (2002) 1–19, http://dx.doi.org/10.1680/gein.9.0208.

[5] D. Walters, T. Allen, R. Bathurst, Conversion of geosynthetic strain to load using reinforcement stiffness, Geosynth. Int. 9 (5–6) (2002) 483–523, http://dx.doi.org/10.1680/gein.9.0226.

[6] M. Al-Barqawi, R. Aqel, M. Wayne, H. Titi, R. Elhajjar, Polymer geogrids: A review of material, design and structure relationships, Materials 14 (16) (2021) 4745, http://dx.doi.org/10.3390/ma14164745.

[7] P. Shen, J. Han, J.G. Zornberg, A.M. Morsy, D. Leshchinsky, B.F. Tanyu, C. Xu, Two and three-dimensional numerical analyses of geosynthetic-reinforced soil GRS piers, Geotext. Geomembr. 47 (3) (2019) 352–368, http://dx.doi.org/10.1016/j.geotexmem.2019.01.010.

[8] J. Chen, X. Guo, R. Sun, S. Rajesh, S. Jiang, J. Xue, Physical and numerical modelling of strip footing on geogrid reinforced transparent sand, Geotext. Geomembr. 49 (2) (2021) 399–412, http://dx.doi.org/10.1016/j.geotexmem.2020.10.011.

[9] J. Huang, J. Han, J.G. Collin, Geogrid-reinforced pile-supported railway embankments: A three-dimensional numerical analysis, Transp. Res. Rec. 1936 (1) (2005) 221–229, http://dx.doi.org/10.1177/0361198105193600125.

[10] K. Hatami, R.J. Bathurst, Development and verification of a numerical model for the analysis of geosynthetic-reinforced soil segmental walls under working stress conditions, Can. Geotech. J. 42 (4) (2005) 1066–1085, http://dx.doi.org/10.1139/t05-040.

[11] G. Leonardi, F. Suraci, A 3D-FE model for the rutting prediction in geogrid reinforced flexible pavements, Sustainability 14 (6) (2022) 3695, http://dx.doi.org/10.3390/su14063695.

[12] B. Saad, H. Mitri, H. Poorooshasb, 3D FE analysis of flexible pavement with geosynthetic reinforcement, J. Transp. Eng. 132 (5) (2006) 402–415, http://dx.doi.org/10.1061/(ASCE)0733-947X(2006)132:5(402).

[13] Y. Zhuang, K. Wang, Three-dimensional behavior of biaxial geogrid in a piled embankment: numerical investigation, Can. Geotech. J. 52 (10) (2015) 1629–1635, http://dx.doi.org/10.1139/cgj-2014-0538.

[14] M. Hussein, M. Meguid, A three-dimensional finite element approach for modeling biaxial geogrid with application to geogrid-reinforced soils, Geotext. Geomembr. 44 (3) (2016) 295–307, http://dx.doi.org/10.1016/j.geotexmem.2015.12.004.

[15] I. Amirhosseini, V. Toufigh, M.M. Toufigh, E. Ghazavi-Baghini, Three-dimensional modeling of geogrid pullout test using finite-element method, Int. J. Geomech. 22 (3) (2022) 04021297, http://dx.doi.org/10.1061/(ASCE)GM.1943-5622.0002218.

[16] H. Liu, H. Ling, Modeling cyclic behavior of geosynthetics using mathematical functions combined with masing rule and bounding surface plasticity, Geosynth. Int. 13 (6) (2006) 234–245, http://dx.doi.org/10.1680/gein.2006.13.6.234.

[17] A. Sawicki, A basis for modelling creep and stress relaxation behaviour of geogrids, Geosynth. Int. 5 (6) (1998) 637–645, http://dx.doi.org/10.1680/gein.5.0139.

[18] D. Hirakawa, W. Kongkitkul, F. Tatsuoka, T. Uchimura, Time-dependent stress–strain behaviour due to viscous properties of geogrid reinforcement, Geosynth. Int. 10 (6) (2003) 176–199, http://dx.doi.org/10.1680/gein.10.6.176.37246.

[19] R. Bathurst, V. Kaliakin, Review of numerical models for geosynthetics in reinforcement applications, in: Computer Methods and Advances in Geomechanics: 11th International Conference of the International Association for Computer Methods and Advances in Geomechanics, Vol. 4, Torino, Italy, 2005, pp. 407–416.

[20] G. Lombardi, A.M. Paula, M. Pinho-Lopes, Constitutive models and statistical analysis of the short-term tensile response of geosynthetics after damage, Constr. Build. Mater. 317 (2022) 125972, http://dx.doi.org/10.1016/j.conbuildmat.2021.125972.

[21] ABAQUS, ABAQUS/Standard User's Manual, Version 2021, Dassault Systèmes Simulia Corp, 2021.

[22] ISO-10319, BS EN ISO 10319:2015: Geosynthetics – Wide-Width Tensile Test, BSI Standards Limited, 2015.

[23] M. Pinho-Lopes, A.M. Paula, M.L. Lopes, Pullout response of geogrids after installation, Geosynth. Int. 22 (5) (2015) 339–354, http://dx.doi.org/10.1680/jgein.15.00016.

[24] M.F. Pinho-Lopes, M.L. Lopes, Influence of mechanical damage induced in laboratory on the soil-geosynthetic interaction in inclined-plane shear, Constr. Build. Mater. 185 (2018) 468–480, http://dx.doi.org/10.1016/j.conbuildmat.2018.07.094.

[25] F.N. Fritsch, J. Butland, A method for constructing local monotone piecewise cubic interpolants, SIAM J. Sci. Stat. Comput. 5 (2) (1984) 300–304, http://dx.doi.org/10.1137/0905021.

[26] P. Virtanen, R. Gommers, T.E. Oliphant, M. Haberland, T. Reddy, D. Cournapeau, E. Burovski, P. Peterson, W. Weckesser, J. Bright, et al., SciPy 1.0: fundamental algorithms for scientific computing in Python, Nat Methods 17 (3) (2020) 261–272, http://dx.doi.org/10.1038/s41592-019-0686-2.

[27] Z. Qi, N. Hu, G. Li, D. Zeng, X. Su, Constitutive modeling for the elastic-viscoplastic behavior of high density polyethylene under cyclic loading, Int. J. Plast. 113 (2019) 125–144, http://dx.doi.org/10.1016/j.ijplas.2018.09.010.

[28] F. Irgens, Continuum Mechanics, Springer Science & Business Media, 2008.

[29] J. Salençon, Handbook of Continuum Mechanics: General Concepts Thermoelasticity, Springer Science & Business Media, 2012.

[30] F. Dunne, N. Petrinic, Introduction to Computational Plasticity, OUP Oxford, 2005.

[31] A. Hillerborg, M. Modéer, P.E. Petersson, Analysis of crack formation and crack growth in concrete by means of fracture mechanics and finite elements, Cem. Concr. Res. 6 (6) (1976) 773–781, http://dx.doi.org/10.1016/0008-8846(76)90007-7.